ACS APPLIED MATERIALS & INTERFACES

Research Article

www.acsami.org

Dielectric Characterization of Confined Water in Chiral Cellulose Nanocrystal Films

Bharath Natarajan,[†,‡] Caglar Emiroglu,[†,‡] Jan Obrzut,[*,†] Douglas M. Fox,[§] Beatriz Pazmino,[†] Jack F. Douglas,[†] and Jeffrey W. Gilman[†]

[†]Material Measurement Laboratory, National Institute of Standards and Technology, Gaithersburg, Maryland 20899, United States

[‡]Department of Physics, Georgetown University, Washington, D.C. 20057, United States

[§]Department of Chemistry, American University, Washington, D.C. 20016, United States

Supporting Information

ABSTRACT: A known deterrent to the large-scale development and use of cellulose nanocrystals (CNCs) in composite materials is their affinity for moisture, which has a profound effect on dispersion, wetting, interfacial adhesion, matrix crystallization, water uptake, and hydrothermal stability. To quantify and control the hydration and confinement of absorbed water in CNCs, we studied sulfated-CNCs neutralized with sodium cations and CNCs functionalized with less hydrophilic methyl(triphenyl)phosphonium cations. Films were cast from water suspensions at 20 °C under controlled humidity and drying rate, yielding CNC materials with distinguishably different dielectric properties and cholesteric structures. By controlling the evaporation rate, we obtained self-assembled chiral CNC films with extended uniformity, having helical modulation length (nominal pitch) tunable from 1300 to 600 nm. SEM imaging and UV−vis−NIR total reflectance spectra revealed tighter and more uniform CNC packing in films cast at slow evaporation rates or having lower surface energy when modified with phosphonium. The dielectric constant was measured by a noncontact microwave cavity perturbation method and fitted to a classical mixing model employing randomly oriented ellipsoidal water inclusions. The dielectric constant of absorbed water was found to be significantly smaller than that for free liquid indicating a limited mobility due to binding with the CNC "matrix". In the case of hydrophilic Na-modified CNCs, a decreasing pitch led to greater anisotropy in the shape of moisture inclusions (ellipsoidal to platelet-like) and greater confinement. In contrast, the structure of hydrophobic phosphonium-modified CNC films was found to have reduced pitch, yet the shape of confined water remained predominantly spherical. These results provide a useful perspective on the current state of understanding of CNC−water interactions as well as on CNC self-assembly mechanisms. More broadly, we believe that our results are beneficial for the realization of CNC-based functional materials and composites.

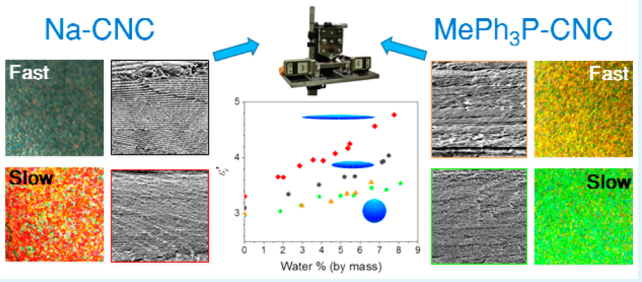

KEYWORDS: *cellulose nanocrystals, self-assembly, water confinement, dielectric properties, chiral nematic structure*

1. INTRODUCTION

Cellulose nanocrystals (CNCs) are fundamental backbones of macroscopic polymeric cellulosic fibers. In nature, cellulose is synthesized from glucopyranose molecules by a combined action of biopolymerization, spinning, and crystallization—all controlled by specific enzymatic terminal complexes in aqueous environment. CNCs can be isolated from cellulose fibers by preferential acid hydrolysis of paracrystalline regions, which leaves highly crystalline CNCs intact.[1] In CNCs, cellulose chains are tightly packed together into rod-like crystallites, which are stabilized by van der Waals forces and by a strong and complex intra- and intermolecular hydrogen-bond network. The typical cross-sectional width of CNCs is in the range of a few nanometers while their average length exceeds 100 nm (aspect ratios span 10−150).[2] Their mechanical properties exceed any known natural or synthetic biomaterial (modulus ≈ 150 GPa, strength ≈ 1.6−3 GPa).[3,4] The high modulus and aspect ratio, in combination with other favorable intrinsic properties such as high surface-to-volume ratios, crystallinity, and low density (1.62 g/cm^3), make CNCs excellent candidates for sustainable reinforcing materials in polymer nanocomposites.[5,6] These attractive properties have motivated numerous endeavors toward fabricating multifunctional CNC nanocomposites using solution casting, melt processing, sol−gel, and template methods,[1,5,7] which may yield the typical low filling fraction nanocomposites (<40 mass %) or highly filled biomimetic composites with cholesteric self-assembled CNCs.[8,9]

Irrespective of the final composite form, one of the key hindrances to the realization of the potential promised by CNC

Received: February 3, 2017
Accepted: April 10, 2017
Published: April 10, 2017

DOI: 10.1021/acsami.7b01674
ACS Appl. Mater. Interfaces XXXX, XXX, XXX−XXX

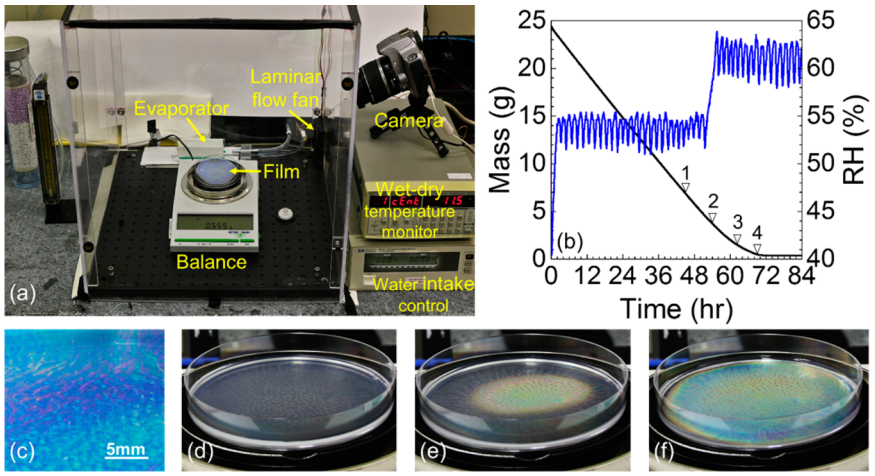

Figure 1. (a) CNC-film casting setup. (b) Plots of the suspension mass and humidity (RH) versus drying time. Markers 1−4 correspond to formation of the macroscopic substructures shown in images c−f. The pattern of the self-assembled substructure at (image c) remains fixed throughout the rest of the drying process. (d−f). To avoid film cracking, humidity inside the chamber is increased to 60% at the marker point 2 (images captured at angle of 30° to film surface, through a circular polarizer attached to the camera lens).

fillers is moisture. CNCs are synthesized in aqueous media, and as-synthesized CNCs are found to disperse only in water and high dielectric constant solvents due to restrictions imposed by their high surface charge. Given this difficulty, CNC nanocomposites are most readily prepared by solution casting CNC−polymer−water mixtures. Because of their hydrophilic nature and high surface area, CNCs display a tendency to retain a hard-to-remove surface layer of water, even when functionalized and/or solvent exchanged into nonpolar solvents.[7,10] Dried CNC powders, which are starting materials in melt mixing and extrusion, rapidly absorb atmospheric moisture prior to incorporation. This layer of water may diminish the CNC−matrix and CNC−CNC adhesion, particularly in hydrophobic matrices, where CNCs are found to promote water uptake and serve as conduits for water transport.[11−13] Sinko and Keten observed the CNC−CNC shear modulus to decrease by 2 orders of magnitude in going from a dry to wet interface.[12] The competitive hydrogen bonding of CNCs with water was additionally found to cause a disruption in percolated CNC networks, resulting in ineffective stress transfer and remarkable material softening.[13] The presence of interfacial water is also likely to hinder or promote the crystallization of semicrystalline host polymers.[14] The increased presence of water can be a technological problem when the polymer properties and dimensions are sensitive to solvent molecules. It is therefore key to understand the interaction of water with cellulose nanocrystals.[7]

CNCs derived from natural cellulose sources via acid hydrolysis can self-assemble into a stable chiral-nematic liquid crystalline phase, although the extent of ordering is often limited by vitrification during the course of film drying. The chiral-nematic (cholesteric) phase model often used to describe these materials shows a long-range orientation of individual CNC rods with characteristic helical modulation length perpendicular to the direction of their alignment.[15] In the CNC films the local helical alignment (nominal "pitch") can be in the submicron range, resulting in often spectacular Bragg reflection in visible light and a quasi-photonic band gap.[15] As it is in many living organisms, the helical organization of CNCs can lead to bio-inspired materials with efficient dissipation of the fracture energy, with extremely large damage tolerance and hindered catastrophic crack propagation.[16] However, from the point of view of this paper, they serve as model films with known crystallinity and mesostructure that help gain understanding of CNC water interactions and water confinement in CNCs.

In this work, we study CNCs films of two different surface functionalities (sodium and methyl(triphenyl)phosphonium cations), cast from water dispersions at 20 °C, under controlled humidity and drying rate to obtain nanocrystals organized into well-defined distinguishably different chiral structures with characteristic helical modulation length (pitch). A noncontact microwave cavity perturbation method enabled permittivity measurements with accuracy adequate to study water confinement in CNCs. Complementary characterization included SEM imaging, UV−vis−NIR chiral dichroism (CD), and reflectance spectra. We find that tuning the evaporation rate can control the helical pitch and uniformity of the cholesteric films. Our results indicate that moisture inclusions assume ellipsoidal shapes when the helical pitch is larger than 1200 nm. When the pitch decreases, the shape becomes more anisotropic, and eventually, at about 700 nm, water inclusions assume a needle or platelet-like shape. For hydrophobic phosphonium modified CNC films, with weaker water−CNC interactions, the pitch was found to have a diminished effect on the water shape. We discuss the underlying mechanism of liquid crystalline gelation and helical ordering of CNCs, which offer useful perspective on the current state of understanding of CNCs materials and can be beneficial for the realization of CNC functional materials and composites.

2. EXPERIMENTAL SECTION

2.1. Materials. Sulfated CNCs neutralized to a sodium form (Na-CNC) were obtained from the University of Maine Process Development Center as an aqueous suspension at 11.9 mass %. TEM and AFM measurements revealed that the CNCs had an average diameter of 5.9 ± 1.8 nm and length of 130 ± 67 nm.[2] Methyl(triphenyl)phosphonium bromide (98%) was obtained from Merck. The Na-CNCs were functionalized with methyl(triphenyl)-phosphonium cations ($MePh_3P$-CNC) by a facile ion exchange chromatographic technique described elsewhere.[17]

2.2. Preparation of Solid CNC Films. Films of Na- and $MePh_3P$-CNCs were cast from 1.5 mass % CNC−water suspensions in a 60

DOI: 10.1021/acsami.7b01674
ACS Appl. Mater. Interfaces XXXX, XXX, XXX−XXX

mm diameter polystyrene Petri dish inside a sealed Plexiglas chamber (Figure 1a). The chamber was equipped with a computer-connected microbalance and evaporation pad with a computer-controlled DI water supply and provided with purified dry air having relative humidity (RH) of 20% and a temperature of 20 ± 0.5 °C. The mass of the CNC suspension and the RH inside the chamber were continuously monitored. The desired drying rate profile was obtained by using a computer algorithm actively adjusting the RH inside the chamber. We note that tracking the mass loss (gradient) is a more reliable approach in controlling the film structure compared to purely monitoring the temperature, RH, or refractive index.[18,19] An example of mass loss of representative CNC suspension and the corresponding RH required to maintain the desired drying rate is shown in Figure 1b.

During the drying process, the suspension transitions from a structureless, clear mixture to one with a macroscopic surface patterns (Movie S1). This is attributed to the large-scale assembly of CNCs into a cholesteric phase in the film bulk, a process which requires surface reorganization. Figure 1c shows an image during drying where this gel-like CNC self-assembly emerges from the suspension. This transition is observed to happen at a CNC concentration of ≈4.5 mass %, which is in general agreement with previously measured biphasic to liquid crystal transition mass fractions.[20,21] It is noteworthy that the large scale self-assembly pattern seen in Figure 1c remains fixed throughout the rest of the film drying process (Figure 1d–f). The evaporation in our CNC solutions proceeds from the center to the outer edges, as opposed to the coffee-stain drying seen in cast drops.[22] As the drying front progresses outward, the meniscus becomes less parallel to the bottom of the Petri dish creating a large degree of nonuniformity in the outer regions of the film (Figure S1). Thus, the uniform central region is used for measurements.

2.3. Dielectric Characterization. The complex relative permittivity ($\varepsilon_r = \varepsilon_r' - j\varepsilon_r''$) of the CNC films was measured at a frequency of 7.435 GHz using a noncontact cavity perturbation method,[23,24] which allows precise measurement of the dielectric permittivity in quantitative correlation with the moisture content. This method is nondestructive and experimentally simple, and it does not require any electrical contacts that would otherwise obscure the water absorption and its effect on the dielectric properties of CNCs.

In our earlier work[23,24] we showed that for a small specimen inside a rectangular cavity operating in the TE_{10n}, the classical perturbation equation[25] can be simplified to linear analytic expressions:

$$y' = (\varepsilon_r' - 1)2x - b' \quad (1a)$$

$$y'' = \varepsilon_r''4x - 2b'' \quad (1b)$$

Parameters x, y', and y'' in the linear equations (1) are defined as follows:

$$x = V_s/V_0, \quad y' = (f_0/f_s)/f_0, \quad y'' = 1/Q_s - 1/Q_0 \quad (2)$$

where f_0 = 7.4355 GHz is the resonant frequencies of the empty cavity, f_s is the resonant frequency with the specimen, V_0 is the volume of the cavity, and V_s is the volume of the specimen ($V_0 \gg V_s$). Q_0 is the quality factor of the empty cavity, and Q_s is the quality factor of the cavity loaded with the specimen. The quality factor is obtained from the resonant peak according to the conventional half power bandwidth formula as $Q_s = f_s/\Delta f_s$. The real permittivity ε_r' and the dielectric loss ε_r'' can be determined from the slope of eqs (1), where intercepts b' and b'' are constant (Figure 2c). Our cavity test fixture design shown in Figure 2a employs a 127 mm long WR90 waveguide, operating in the microwave frequency range of 6.7–13 GHz. The fixture is connected to a network analyzer (Agilent N5225A) with semirigid coaxial cables and near cross-polarized coaxial to WR90 coupling adapters. The network analyzer measures the transmission scattering parameter $\mathbf{S}_{21}$. The resonant frequency, f_s, and the half power bandwidth, Δf_s, are determined for the TE_{103} resonant mode.

The specimen is inserted into the cavity through a slot in the center of the cavity, where the electric field of the resonant mode, TE_{103}, attains a maximum value. The specimen insertion and the corresponding volume of the material in the cavity (V_s) are controlled by a stage. During the measurements, the specimen is partially inserted in steps, while the magnitude of the scattering parameter, $\mathbf{S}_{21}$, is recorded. The measured frequency span is typically $2\Delta f_s$, recorded with a resolution of ±50 kHz. The dynamic range of the noise level in the $|\mathbf{S}_{21}|$ magnitude is typically below −65 dB. Figure 2b shows the evolution of the resonant peak at the indicated moisture levels at fixed CNC specimen volume inside the cavity. The corresponding plots of eq 1a are shown in Figure 2c, where the slope of the plots equals to $\varepsilon_r' - 1$. Similarly, eq 1b can be used to estimate the dielectric loss, ε_r''. The dielectric constant is determined with the combined relative uncertainty of 3%.

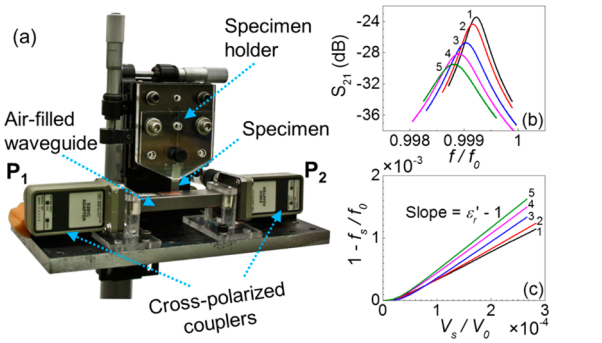

Figure 2. (a) Microwave cavity test fixture. Ports P_1 and P_2 are connected to a network analyzer. (b) Evolution of the TE_{103} resonant peak with increasing water content indicated by (1) 0%, (2) 2.1%, (3) 5.0%, (4) 6.0%, and (5) 7.3%. (c) Plots of eq 1a as a function of specimen volume, V_s. The slopes of the linear plots correspond to $\varepsilon_r' - 1$, and they increase with increasing water content in the CNC films.

2.4. Optical Characterization. The optical microscopy images were obtained in a polarized optical microscope using a 5× objective with numerical aperture (NA) = 0.13. The imaging was performed with a cross-polarization setting to ensure that only the circularly polarized component of the reflected light was collected.

The total reflectance and transmittance spectra were recorded from 200 to 2000 nm with a 1 nm step resolution and at slit widths between 4 and 10 nm using a PerkinElmer Lambda 950 spectrophotometer equipped with an integrating sphere kit for Lambda 950. By measuring the total reflectance (R) and transmittance (T), we verified that $R + T$ sum to 1; i.e., absorption is negligibly small, and therefore R and T are complementary to each other. Consequently, we only measured the reflectance of the CNC films using the spectrophotometer. The combined relative uncertainty in determining the peak wavelength from the Bragg reflection maximum is ±5 nm.

2.5. SEM Imaging. Fracture cross sections of the dried CNC films were imaged using a FEI Helios dual-beam focused ion beam (FIB)/scanning electron microscope (SEM). The samples were scanned using an electron beam at a voltage of 2 kV and a current of 50 pA and imaged using a highly sensitive, high-performance ion conversion and electron (ICE) secondary electron (SE) detector. A working distance of 4 mm was used. The samples were imaged without a conductive coating at a pixel size of 15–30 nm. In order mitigate charging effects, a stage bias of 50 V was applied, and the images were acquired by integrating 16 500 ns scans. When imaging the sample cross sections, the regions in the field of view were verified to be roughly planar and perpendicular to the optic axis to minimize the effect of large height variations on final quantification. Unlike several earlier studies, we obtained images at low and high magnifications to ensure that the measurements are accurate as well as statistically representative.

3. RESULTS AND DISCUSSION

3.1. Dielectric Properties. The dielectric constant of the films was measured at 7.435 GHz using the method described in section 2.3. For this purpose, specimens of CNC films, size of 8 mm × 15 mm and between 30 and 60 μm thick, were cut from the freshly cast films that typically contain 5 mass % of

DOI: 10.1021/acsami.7b01674
ACS Appl. Mater. Interfaces XXXX, XXX, XXX–XXX

water. Water concentration was determined gravimetrically by weighing the specimens on an ultra-microbalance (MSE2.7S-000-DM from Sartorius) with a readability of 0.1 μg. The initial water content was determined by drying films to constant mass at 120 °C for several hours inside of a glovebox under argon dry atmosphere (water content <6 ppm). By re-exposing CNC to humid air, the water concentration within CNCs was varied from about 0 to about 9 mass %. At different time intervals during the adsorption, moisture content in the samples was determined gravimetrically, and cavity measurements were performed at room temperature (20 °C). The measured dielectric constant for slow and fast-dried Na-CNC and $MePh_3P$-CNC films are shown in Figure 3 and summarized

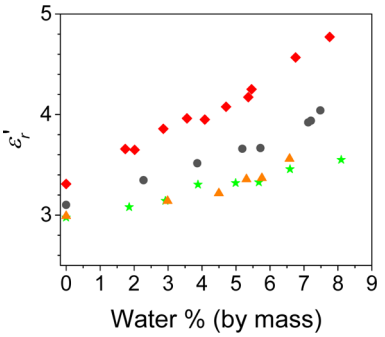

Figure 3. Dielectric constant (ε_r') of CNC films as a function of water content. Square symbols: slow-dried Na-CNC; circles: fast-dried Na-CNC; triangles: fast-dried $MePh_3P$-CNC; stars: slow-dried $MePh_3P$-CNC.

Table 1. Dielectric Constant Values of CNC Films at 0 and 5 mass % of Water

material	drying rate	ε_r' at 0 mass % of water	ε_r' at 5 mass % of water
Na-CNC	(slow 7 mg/min)	3.31	4.12
Na-CNC	fast (13 mg/min)	3.10	3.66
$MePh_3P$-CNC	slow (7 mg/min)	2.98	3.33
$MePh_3P$-CNC	fast (13 mg/min)	2.99	3.36

in Table 1. Figure 3 demonstrates that with increasing water content the dielectric constant of CNC films increases. Our results show, however, that the change in the dielectric constant depends on the drying rate and the chemical modification of CNCs. The dielectric constant of Na-CNC films dried slowly is considerably larger compared to films dried at faster rates. At a water mass content of 5%, decreasing the drying rate from 13 to 7 mg/min increases the dielectric constant from 3.3 to 4.1. In comparison, at the corresponding water concentration, the dielectric constant of phosphonium-modified $MePh_3P$-CNC films is smaller and evidently much less dependent on the drying rate (Table 1).

Estimating the dielectric property of mixtures has been a challenging field of research, of both theoretical and practical importance. The classical mixing approach is to consider homogeneous inclusions (water) in an isotropic host medium (CNCs), within the linear range of molecular polarization of such inclusions. The quasi-static nature of the modeling means that the propagating wavelength in a mixture is to be considered much larger than the inclusion diameter for a satisfactory dynamic field approximation.[26] Within this assumption, one can model the CNC−water mixture as an ideal two phase mixture. We note that earlier studies have found water uptake into CNC films to be due to penetration between the crystals rather than the swelling of individual nanocrystals, as water does not permeate into the crystal structure.[27] These results lend support to our treatment of water as an inclusion in a "matrix" of CNCs. In the simplest model of this kind, the water inclusions are spherical in shape. A more general approach allows for arbitrary shapes, but the concentration of the inclusions must be assumed to be small within the simplifying assumption that the dielectric constant of the dispersed water is much higher than the CNC "matrix". The change of the dielectric constant can be calculated to high accuracy numerically for particles of essentially any shape,[28] but regular shapes, such as ellipsoids, simply allow for closed analytical estimates of the change in the dielectric constant in this dilute regime.[29,30]

We consider randomly oriented ellipsoidal inclusions with semiaxial dimensions a_x, a_y, a_z and depolarization factors N_x, N_y, N_z along x, y, z directions, respectively, in the Cartesian coordinate system. Any point on the surface of the ellipsoid is given by eq 3:

$$\frac{x^2}{a_x^2} + \frac{y^2}{a_y^2} + \frac{z^2}{a_z^2} = 1 \tag{3}$$

Depolarization factors (N_j) are descriptors of the extent to which the inclusion polarization is diminished according to the particle's shape and orientation with respect to the applied electric field. Following the Maxwell−Garnett model for such shape modification, the expression for the effective dielectric permittivity of the mixture ε_{eff} is then given by eq 4:

$$\varepsilon_{eff} = \varepsilon_{CNC} + \varepsilon_{CNC}\frac{f\sum_{j=x,y,z}\frac{\varepsilon_{water}-\varepsilon_{CNC}}{\varepsilon_{CNC}+N_j(\varepsilon_{water}-\varepsilon_{CNC})}}{3 - f\sum_{j=x,y,z}\frac{N_j(\varepsilon_{water}-\varepsilon_{CNC})}{\varepsilon_{CNC}+N_j(\varepsilon_{water}-\varepsilon_{CNC})}} \tag{4}$$

where f is the volumetric inclusion ratio, ε_{water}, is the permittivity of water, and ε_{CNC} is the permittivity of the CNC film at 0% water. According to ref 31, the depolarization factors for any given ellipsoid are equal to (5):

$$N_j = \frac{a_x a_y a_z}{2}\int_0^\infty \frac{du}{(u+a_j^2)\sqrt{(u+a_x^2)(u+a_y^2)(u+a_z^2)}}, \quad j = x, y, z \tag{5}$$

with $N_x + N_y + N_z = 1$. In the case of a sphere, $N_x = N_y = N_z = 1/3$.

Solutions of (5) for prolate ($a_z > a_x = a_y$) and oblate spheroids ($a_z < a_x = a_y$) are given by eqs 6 and 7, respectively:

$$N_z = \frac{1-e^2}{2e^3}\left(\ln\frac{1+e}{1-e} - 2e\right), \quad e = \sqrt{1 - \frac{a_x^2}{a_z^2}} \tag{6}$$

$$N_z = \frac{1+e^2}{e^3}(e - \tan^{-1} e), \quad e = \sqrt{\frac{a_x^2}{a_z^2} - 1} \tag{7}$$

The axial parameters of water inclusions are obtained here by fitting the measured dielectric constant against eq 4 with ε_{water} and a_x/a_z in eq 7 as the fitting parameters, where $a_x = a_y = a_z$

DOI: 10.1021/acsami.7b01674
ACS Appl. Mater. Interfaces XXXX, XXX, XXX−XXX

for spherical shape of water inclusions and $a_x = a_y > a_z$ for all cases of oblate spheroids.

In the case of hydrophobic $MePh_3P$-CNC films, which show the lowest dielectric constant values, we initially fit the dielectric data to eq 4 assuming simple spherical shape for water inclusions. In our experiment, at the frequency of 7.435 GHz, $\varepsilon_{water} = 65$, which is the dielectric constant value of unbound liquid water with a relaxation time $\tau_{free} \approx 9.3$ ps.[32] However, these initially calculated ε_{eff} values from eq 4 are too high compared to the experimental data (see Figure S2). Since the Maxwell–Garnett theory gives the lowest ε_{eff} values of the mix for spherical shape inclusion, these fitting results have no physical meaning under assumption of free water in the mixture. Considerably better fits, however, can be obtained with $\varepsilon_{water} < 65$. The decreased value of ε_{water} indicates that, in comparison to free water, water in CNCs has a limited mobility and consequently longer relaxation time due to bounding with CNC matrix. In Figure S2 we show a good agreement between fitting results and experimental data when $\varepsilon_{water} = 33$, indicating that degree of water interaction with CNCs is significant. This effect is qualitatively similar to immobilization of water molecules in ice or under internal electrical field from surrounded polar molecules,[32,33] where the dielectric dispersion is shifted to lower frequencies or longer relaxation time. The relaxation time of water bound to CNCs can be estimated from the Cole–Cole dispersion model (8) for water[32] by using the observed decrease in the dielectric constant of water from 65 to 33 at the fixed frequency of 7.435 GHz:

$$(\varepsilon_r' - j\varepsilon_r'')_\omega - \varepsilon_\infty = (\varepsilon_s - \varepsilon_\infty)/(1 + (j\omega\tau)^{1-\alpha}) \quad (8)$$

where ε_r' and ε_r'' are the frequency-dependent real and imaginary parts of the complex permittivity, ε_s and ε_∞ are relaxed (static) and unrelaxed values of the dielectric constant, respectively, τ is the dielectric relaxation time, $\omega = 2\pi f$ is the angular frequency, and $j^2 = -1$. Assuming after ref 32 $\varepsilon_s = 78$, $\varepsilon_\infty = 4.23$, $\tau \approx 9.3$ ps, and $\alpha = 0.013$, we estimate from eq 8 the relaxation time of bound water in CNCs, $\tau_{bound} \approx 24$ ps, nearly 3 times longer than that of liquid free water (see Figure S3).

In addition to the water immobilization effect, the measured ε_{eff} shows considerable dependence on the water inclusion shape. Since in our experiment the water concentration in CNCs is relatively low, it is convenient to examine the shape of the confined water by plotting the results of fitting to Maxwell–Garnett model using the permittivity–susceptibility ratio (SR) notation. The generalized effective mixture SR[30] for a given volumetric ratio is defined by eq 9.

$$SR = (\varepsilon_{eff} - \varepsilon_{CNC})/(\varepsilon_{water} - \varepsilon_{CNC}) \quad (9)$$

The fits to the change in SR as a function of water content are shown in Figure 4. From the slope of SR plots in Figure 4 we deduce that in the slowly dried Na-CNC films the axial parameters ratio of ellipsoidal water, a_x/a_z, approach the value of about 30, indicating nearly flattened water. In the case of the fast dried Na-CNCs, a_x/a_z decreases to about 6, which corresponds to an ellipsoid with a lower aspect ratio. And finally, for the phosphonium-modified CNCs the axial parameters of confined water are consistent with the spherical shape. These shapes are illustrated in Figure 4. The measured difference in water confinement between the specimens dried at different rates can be attributed to the degree of chiral ordering in the films as well as the surface functionality, which we discuss in the following sections.

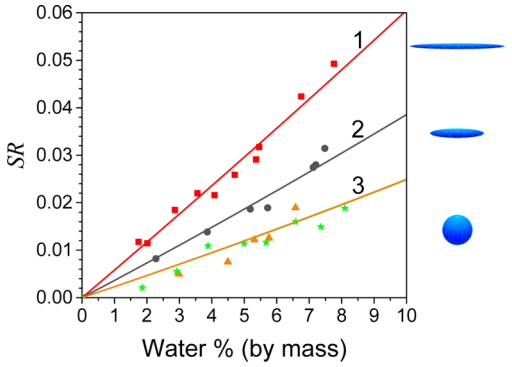

Figure 4. Dielectric susceptibility ratio (SR) as a function of water concentration. Lines represent fitting to eq 9 through the data points. Square symbols: slow-dried Na-CNC; circles: fast-dried Na-CNC; triangles: fast-dried $MePh_3P$-CNC; stars: slow-dried $MePh_3P$-CNC. Water confinement shapes corresponding to plots 1–3 have axial ratios a_x/a_z = 30, 6, and 1, respectively. They are illustrated on the right as distinct pancake-like oblate ellipsoidal shapes for Na-CNCs and as a sphere for phosphonium-modified CNCs.

3.2. CNC Film Structure. To understand the role of the evaporation kinetics and functionalization on the structure and thence the effect of the structure on water confinement, we characterized, in detail, the self-assembled architecture of the CNC films using polarized optical microscopy (POM), UV–vis–NIR reflectance spectroscopy, and SEM. The CNC films imaged using POM display multicolored structures with dominant colors varying based on evaporation conditions and functionalization as shown in Figure 5. Most notably, the fast-dried Na-CNC films are colorless.

The peak reflectance wavelengths (λ) and widths ($\Delta\lambda$) were obtained by fitting the spectrophotometry data using single or multi-Gaussian distributions, as deemed appropriate (Figure 6f). It is observed that the reflectance peaks are consistently narrower and at lower wavelengths when the films are cast at slower evaporation rates (Table 2). This effect is larger for Na-CNCs where slow drying decreases λ_1 from 1274 ± 149 nm to 736 ± 118 nm to 517 ± 98 nm for evaporation rates of 13, 7, and 4 mg/min, respectively. In contrast, slowing the evaporation rate blue-shifts the λ_1 of the $MePh_3P$-CNC films from 655 ± 279 nm to 580 ± 175 nm. However, even the fast-dried $MePh_3P$-CNC films show a comparable peak wavelength to the slow-dried Na-CNC films. The peak reflectance values agree with the structural colors seen in the POM images (Figure 5). The fast-dried Na-CNC films are colorless as they reflect well above the IR range. The reflectance spectra for the fast-dried films also display subcomponent structures with shoulders at longer wavelengths (λ_2, Table 2), hinting at the presence of multiple domains with different nominal pitch (P, assuming a chiral-nematic description of our material).

All the SEM images shown in Figure 6a–e display a periodic pattern, characteristic of chiral nematic self-assembly. These patterns consist of alternating "hills" and "valleys" that correspond to the CNCs oriented parallel and perpendicular to the fracture surface, respectively (higher magnification images are shown in Figure S5). This structure, which is attributed to the anisotropic pull-out behavior of CNC layers in the film, is key to the quantification of the pitch and orientation.[34] From a visual inspection of the SEM images (Figure 6a–e), it is clear that the faster evaporation rates result in a progressive deviation from an ideal chiral-nematic liquid

DOI: 10.1021/acsami.7b01674
ACS Appl. Mater. Interfaces XXXX, XXX, XXX–XXX

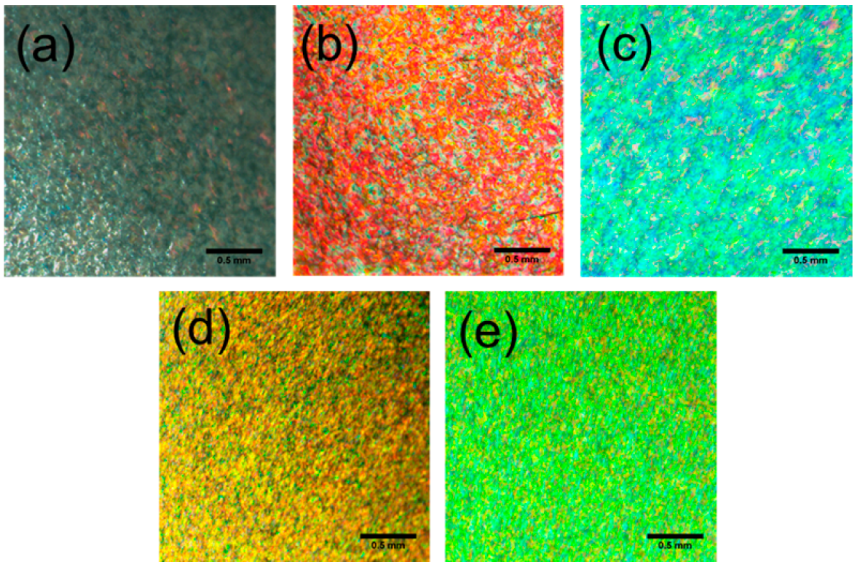

Figure 5. Polarized optical microscopy images of (a) fast-dried Na-CNCs, (b) slow-dried Na-CNCs, (c) slowest-dried Na-CNCs, (d) fast-dried $MePh_3P$-CNC, and (e) slow-dried $MePh_3P$-CNC. The images are obtained in cross-polarization configuration. The scale bars represent 0.5 mm. The image in (a) corresponds to a colorless-transparent film in the optical spectrum range.

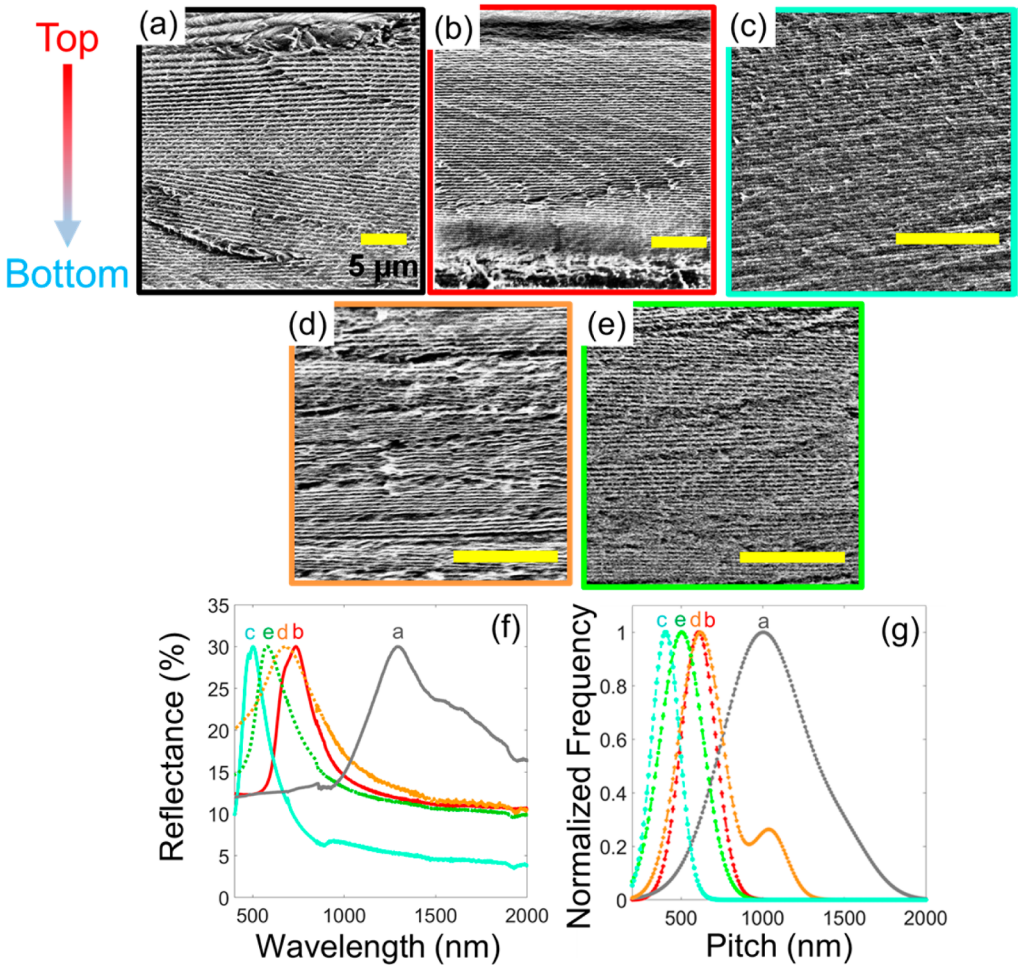

Figure 6. SEM images of the cross section of (a) fast-dried Na-CNCs, (b) slow-dried Na-CNCs, (c) slowest-dried Na-CNCs, (d) fast-dried $MePh_3P$-CNC, and (e) slow-dried $MePh_3P$-CNC. The scale bars represent 5 μm. Images at identical magnification are shown in Figure S6. (f) The corresponding reflectance spectra from the various films. (g) The nominal pitch distributions measured from the SEM images of the various films.

crystal ordering due to film vitrification. For instance, the fast-dried Na-CNC films possess a multidomain structure, with an imperfect planar texture. Specifically, this structure is an ensemble of Bragg-reflecting planar domains, each with a

DOI: 10.1021/acsami.7b01674
ACS Appl. Mater. Interfaces XXXX, XXX, XXX−XXX

Table 2. Reflectance Peak Position (λ) and Peak Widths ($\Delta\lambda$) (Defined at One Standard Deviation throughout the Text) of CNC Films

material	drying rate	λ_1 (nm)	$\Delta\lambda_1$ (nm)	λ_2 (nm)	$\Delta\lambda_2$ (nm)
Na-CNC	slowest (4 mg/min)	517	98		
Na-CNC	slow (7 mg/min)	736	118		
Na-CNC	fast (13 mg/min)	1274	149	1570	270
$MePh_3P$-CNC	slow (7 mg/min)	590	175		
$MePh_3P$-CNC	fast (13 mg/min)	655	279	1097	452

characteristic pitch and helical director orientation (Figure 6a and Figure S4). The individual domains are separated by grain boundary like defects, which are akin to the parabolic focal conics observed by Roman and Gray.[35] Additionally, we observe dislocation defects, only seen in optical images earlier (Figure S4).[34] Strikingly, the slow and slowest dried Na-CNC films are relatively defect-free, single domain systems, extending over several millimeters, with a significantly smaller pitch and greater uniformity. The $MePh_3P$-CNC films exhibit a qualitatively similar dependence on evaporation rate. In addition to pitch variations arising from differences in evaporation rates and surface groups, a gradient in pitch is observed in going from the top to bottom of each film. This gradient is observed to be larger for faster dried films (Figure S9). We note for all films studied here that the structures in the dried state are not representative of "liquid crystalline" assembly in its true sense, as the vitrified films are away from their equilibrium morphologies.

To quantitatively evaluate the inter- and intrasample variations, we measured the pitch distribution of each sample type (Figure 6g) using a novel image processing methodology described in the Supporting Information (Figure S7). As with the reflectance data, the distributions were fit with Gaussians to obtain peak positions and peak widths (one standard deviation, Figure S8 and Table 3). The measured pitch and standard

Table 3. Pitch Peaks and Peak Widths of CNC Films Measured from SEM Images

material	drying rate	P_1 (nm)	ΔP_1 (nm)	P_2 (nm)	ΔP_2 (nm)
Na-CNC	slowest (4 mg/min)	420	74		
Na-CNC	slow (7 mg/min)	606	151		
Na-CNC	fast (13 mg/min)	1000	350	1500	250
$MePh_3P$-CNC	slow (7 mg/min)	504	186		
$MePh_3P$-CNC	fast (13 mg/min)	619	190	1045	149

deviations exhibit an identical dependence on evaporation rate and surface functionality. With decreasing evaporation rates, we measure much smaller P and standard deviations (due to greater sample uniformity). Additionally, the P values measured for the $MePh_3P$-CNC films are considerably lower for the same drying rate. The SEM characterization is also found to be sensitive to the multidomain structure of the fast-dried films. We measure secondary peaks at 1500 and 1045 nm for the fast-dried Na and $MePh_3P$ films, respectively.

The helical pitch distributions of CNC films can be used to calculate the total Bragg reflection spectrum using $\lambda = (P/2)n \sin\theta$,[24] where $n = \sqrt{\varepsilon_r'}$ and θ is the angle of incidence. Since the dielectric constant of CNC films is about 4, the average refractive index $n \approx 2$, the helical pitch distribution corresponds directly to the distribution of the peak reflectance wavelength. While the varied orientations of the domains are expected to cause some broadening of the reflectance peaks, we do not expect this to be a significant effect, since angular deviations are within 7° to 8° (sin 90° = 1, sin 82° = 0.99). Comparing the "spectra" in Figures 6f and 6g and the data in Tables 2 and 3, we find that the calculated pitch distributions (including peak wavelengths and peak widths) are in good agreement with the reflectance. We note that the SEM peak values are somewhat lower than the peak reflectance wavelengths. This is because the reflectance was measured in air as opposed to the SEM images, which were obtained in vacuum. In air, we expect swelling from a small amount of absorbed moisture. This agreement between both the peak positions and peak widths suggests that the broadening of reflectance peaks is due to structural nonuniformities locked-in during film vitrification, which in turn arise from self-assembly kinetics and variations in CNC shapes and size.

3.3. Role of CNC Packing and Functionality on Water Confinement. As noted earlier, the shape of confined water in Na-CNC films deviates significantly from the classical sphere. Given that these films differ only in their mesostructures, we can attribute the variations in water confinement shape in Na-CNCs to the differences in self-assembled morphologies. Na-CNC films from the slow dry process have smaller pitch (606 ± 151 nm) and therefore tighter packing. Further they exhibit a greater degree of uniformity and fewer defects. The fast-dried Na-CNC films contrastingly exhibit a larger pitch (1000 ± 350 nm), i.e., looser packing, as well as a higher density of defects arising from the multidomain structure. The tighter packing and uniformity, which result in smaller interstitial volumes, lead to a greater deviation from a spherical water shape ($a_x/a_z = 30$) in the slow-dried Na-CNCs as compared to the fast-dried films of lower density and larger pitch ($a_x/a_z = 6$). Further, we believe that the compression in shape is magnified by the attractive interactions between the hydrophilic Na-CNCs and water.

In comparison, in the case of less hydrophilic $MePh_3P$-CNCs, interactions with water are apparently weaker, allowing water inclusions to assume a spherical shape ($a_x/a_z = 1$) even with a tighter pitch. In order to discuss this is intriguing effect in more detail, we investigate the surface energies of Na-CNC and $MePh_3P$-CNC materials. The surface energies of Na-CNCs and $MePh_3P$-CNCs have been measured by inverse gas chromatography to be 62 mJ/m^2 (dispersive: 54 mJ/m^2; acid−base: 8 mJ/m^2) and 52 mJ/m^2 (dispersive: 45 mJ/m^2; acid−base: 7 mJ/m^2), respectively.[17] Assuming a water surface energy of 72 mJ/m^2 (dispersive: 22 mJ/m^2; acid−base: 50 mJ/m^2) and using the Owens−Wendt formulation,[37] we find the water contact angles to be 59° and 67° for Na-CNCs and $MePh_3P$-CNCs, respectively. This suggests the presence of a weaker water−CNC interaction for the $MePh_3P$-CNCs, which causes the water to take up a more spherical shape as compared to the Na-CNC films. The lowering of water−CNC interactions with phosphonium functionalization is further supported by earlier studies that found the $MePh_3P$-CNCs and their composites to uptake as well as retain lesser amount of water.[17]

3.4. Effect of Evaporation Rate and Functionality on Self-Assembled Structure. Within each functionalization type, we identify primary causes for variations in structure. The

DOI: 10.1021/acsami.7b01674
ACS Appl. Mater. Interfaces XXXX, XXX, XXX−XXX

first being the interplay between the evaporation and self-assembly kinetics. With water evaporating from the samples, the CNC solution reaches a concentration at which 2D stacks of CNCs[38] form into tactoids or 3D cholesteric domains.[39] With further evaporation the domain size increases and the interdomain distances decrease, eventually leading to tactoid alignment, coalescence, and sedimentation.[39] The aligned tactoids lead to greater uniformity. Unaligned tactoids result in dislocation defects (Figure S4).[39] With further drying, the biphasic to liquid crystal transition concentration is reached. At this point, further movement of CNCs and CNC tactoids is kinetically arrested, and the macroscopic surface features seen in Figure 1c are formed. The above-mentioned processes are accompanied by a decrease in pitch from tens to a few micrometers.[21] Following gelation, the water continues to evaporate, causing a further reduction in pitch to micrometer/submicrometer values. Since the drying process begins at the top of the film, CNC domains at the top are vitrified sooner and therefore are locked into nonequilibrium high pitch, lower density structures. Indeed, the pitch in the top layers of the fast-dried films is comparable to the large pitch observed in CNC gels (≈2 μm, Figure S9).[21] The CNC domains closer to the bottom have more time to reorganize into equilibrium morphologies, resulting in a decreasing pitch gradient from the top surface.[40] This is further aided by the shielding/burying of the water meniscus by the upper vitrified layers.

Since the final film morphology results from the series of processes mentioned above, the nonuniformities developed in earlier stages are cascaded down to the final film structure. With faster drying, the critical process points are reached faster and with base structures that possess a higher degree of disorder. Therefore, in these films greater disorder is perpetuated leading to large pitch values and nonuniformities. We are thus led to believe that the evaporation rate at all stages of drying is critical, particularly prior to gelation. Since the last stage of drying takes place after kinetic arrest, we believe it has a less significant effect, as observed earlier.[19] By controlling the mass loss rate during the entire drying process, we are able to tune the pitch of these films by over 800 nm—one of the largest range of pitch values shown thus far.[18,19]

By functionalizing the CNCs with the phosphonium group, the size of the electrical double layer (EDL), which screens the chiral interaction between CNCs, is significantly reduced as compared to the Na-CNCs.[41] The $MePh_3P$-CNCs therefore experience stronger chiral interactions, leading to a smaller pitch and a blue-shift in the reflectance wavelength. Within the $MePh_3P$-CNCs qualitatively similar effects of evaporation rate are observed. However, as mentioned earlier, the effect of evaporation rate is lowered as $MePh_3P$-CNCs' self-assemble more readily and therefore further progressed in the assembly process at every time step as compared to Na-CNCs. The surface functionality and therefore the surface energy of the CNCs represent a valuable knob to control the self-assembly kinetics of CNCs, helping scale-up cholesteric film production by considerably reducing the processing time.

4. CONCLUSION

It is imperative to understand water−cellulose nanocrystal interactions, as they dictate the performance of CNC polymer nanocomposites. As a first step, we tuned the CNC surface chemistry and evaporation rates to obtain an array of model CNC films of known mesostructure and functionality. We found that the water loss rate strongly dictates the final film structure of all CNC films, with fast dried films displaying looser packing and larger disorder in long-range periodicity as evidenced by SEM images and wider, higher wavelength reflectance peaks.[18] Additionally, we found that increased CNC hydrophobicity leads to tighter film packing due to increased suppression of electrostatic repulsion.

This work represents the first structural confirmation of the effect of drying rate. While our observations confirm previously drawn hypotheses about the effect of evaporation, they also elucidate the minutiae of the evaporation process. For example, we found the disordered films to possess a gradient in pitch from the top of the film to the bottom, which depends on the length of time spent by each CNC layer with liquid water. These results also suggest that air flow may direction be used to obtain patterned films of CNCs in all three dimensions, to realize the graded Bouligand structures seen in crustacean shells[8] or to fabricate naturally sourced metamaterials.

The noncontact resonant microwave cavity method allowed us to accurately determine the complex permittivity in relation to water confinement and chemical modification. Most importantly, since no electrical contact processing is required, the chiral integrity of the CNC films can be preserved, allowing a direct correlation between water confinement and helical pitch measurement. On the basis of the analysis of the dielectric susceptibility ratio, we conclude that the dielectric constant of absorbed water is considerably lower than the dielectric constant of free liquid water, indicating limited mobility and longer relaxation time due to bounding within the CNC matrix. We observe that in CNC films with smaller pitch and tighter packing water molecules are confined to tighter spaces. This leads to deviation from a spherical shape compared to films with lower density and larger pitch. The compression in shape is accompanied by favorable interactions between the hydrophilic Na-CNCs and water. In comparison, water confinement in $MePh_3P$-CNC agrees well with the spherical shaped inclusion model due to larger hydrophobicity of phosphonium groups.

■ ASSOCIATED CONTENT

Supporting Information

The Supporting Information is available free of charge on the ACS Publications website at DOI: 10.1021/acsami.7b01674.

Polarized optical microscopy images of film edges, additional plots of CNC dielectric properties, scanning electron microscopy images of CNC film cross sections, image processing methodology and measurements of CNC pitch (PDF)

Movie S1: time-lapse video of CNC film fabrication (AVI)

■ AUTHOR INFORMATION

Corresponding Author

*(J.O.) E-mail jan.obrzut@nist.gov.

ORCID

Jan Obrzut: 0000-0001-6667-9712

Notes

The authors declare no competing financial interest.

■ ACKNOWLEDGMENTS

This work is supported by the NIST grant for the "Nanoscale investigations of the stress response of interphases" project and

DOI: 10.1021/acsami.7b01674
ACS Appl. Mater. Interfaces XXXX, XXX, XXX−XXX

the NIST Nanomanufacturing project. B.N. acknowledges the support of the Air Force Office of Scientific Research (Award No. F1ATA00236G002). Certain commercial equipment, instruments, software, or materials are identified in order to specify the experimental procedure adequately. Such identification is not intended to imply recommendation or endorsement by the National Institute of Standards and Technology, nor is it intended to imply that the materials or equipment identified are necessarily the best available for the purpose.

REFERENCES

(1) Moon, R. J.; Martini, A.; Nairn, J.; Simonsen, J.; Youngblood, J. Cellulose Nanomaterials Review: Structure, Properties and Nanocomposites. *Chem. Soc. Rev.* **2011**, *40*, 3941−3994.
(2) Sacui, I. A.; Nieuwendaal, R. C.; Burnett, D. J.; Stranick, S. J.; Jorfi, M.; Weder, C.; Foster, E. J.; Olsson, R. T.; Gilman, J. W. Comparison of the Properties of Cellulose Nanocrystals and Cellulose Nanofibrils Isolated from Bacteria, Tunicate, and Wood Processed Using Acid, Enzymatic, Mechanical, and Oxidative Methods. *ACS Appl. Mater. Interfaces* **2014**, *6*, 6127−6138.
(3) Šturcová, A.; Davies, G. R.; Eichhorn, S. J. Elastic Modulus and Stress-Transfer Properties of Tunicate Cellulose Whiskers. *Biomacromolecules* **2005**, *6*, 1055−1061.
(4) Saito, T.; Kuramae, R.; Wohlert, J.; Berglund, L. A.; Isogai, A. An Ultrastrong Nanofibrillar Biomaterial: The Strength of Single Cellulose Nanofibrils Revealed via Sonication-Induced Fragmentation. *Biomacromolecules* **2013**, *14*, 248−253.
(5) Eichhorn, S. J.; Dufresne, A.; Aranguren, M.; Marcovich, N. E.; Capadona, J. R.; Rowan, S. J.; Weder, C.; Thielemans, W.; Roman, M.; Renneckar, S.; Gindl, W.; Veigel, S.; Keckes, J.; Yano, H.; Abe, K.; Nogi, M.; Nakagaito, A. N.; Mangalam, A.; Simonsen, J.; Benight, A. S.; Bismarck, A.; Berglund, L. A.; Peijs, T. Review: Current International Research into Cellulose Nanofibres and Nanocomposites. *J. Mater. Sci.* **2010**, *45*, 1−33.
(6) Habibi, Y.; Lucia, L. A.; Rojas, O. J. Cellulose Nanocrystals: Chemistry, Self-Assembly, and Applications. *Chem. Rev.* **2010**, *110*, 3479−3500.
(7) Klemm, D.; Kramer, F.; Moritz, S.; Lindström, T.; Ankerfors, M.; Gray, D.; Dorris, A. Nanocelluloses: A New Family of Nature-Based Materials. *Angew. Chem., Int. Ed.* **2011**, *50*, 5438−5466.
(8) Wang, B.; Walther, A. Self-Assembled, Iridescent, Crustacean-Mimetic Nanocomposites with Tailored Periodicity and Layered Cuticular Structure. *ACS Nano* **2015**, *9*, 10637−10646.
(9) Cheung, C. C. Y.; Giese, M.; Kelly, J. A.; Hamad, W. Y.; MacLachlan, M. J. Iridescent Chiral Nematic Cellulose Nanocrystal/Polymer Composites Assembled in Organic Solvents. *ACS Macro Lett.* **2013**, *2*, 1016−1020.
(10) Viet, D.; Beck-Candanedo, S.; Gray, D. G. Dispersion of Cellulose Nanocrystals in Polar Organic Solvents. *Cellulose* **2007**, *14*, 109−113.
(11) Posner, R.; Ozcan, O.; Grundmeier, G. Water and Ions at Polymer/Metal Interfaces. In *Design of Adhesive Joints Under Humid Conditions*; da Silva, L. F. M., Sato, C., Eds.; Springer: Berlin, 2013; Vol. 25, pp 21−52.
(12) Sinko, R.; Keten, S. Effect of Moisture on the Traction-Separation Behavior of Cellulose Nanocrystal Interfaces. *Appl. Phys. Lett.* **2014**, *105*, 243702.
(13) Dagnon, K. L.; Shanmuganathan, K.; Weder, C.; Rowan, S. J. Water-Triggered Modulus Changes of Cellulose Nanofiber Nanocomposites with Hydrophobic Polymer Matrices. *Macromolecules* **2012**, *45*, 4707−4715.
(14) Anglès, M. N.; Dufresne, A. Plasticized Starch/Tunicin Whiskers Nanocomposite Materials. 2. Mechanical Behavior. *Macromolecules* **2001**, *34*, 2921−2931.
(15) Lagerwall, J. P. F.; Schütz, C.; Salajkova, M.; Noh, J.; Hyun Park, J.; Scalia, G.; Bergström, L. Cellulose Nanocrystal-Based Materials: From Liquid Crystal Self-Assembly and Glass Formation to Multifunctional Thin Films. *NPG Asia Mater.* **2014**, *6*, e80.
(16) Guarín-Zapata, N.; Gomez, J.; Yaraghi, N.; Kisailus, D.; Zavattieri, P. D. Shear Wave Filtering in Naturally-Occurring Bouligand Structures. *Acta Biomater.* **2015**, *23*, 11−20.
(17) Fox, D. M.; Rodriguez, R. S.; Devilbiss, M. N.; Woodcock, J.; Davis, C. S.; Sinko, R.; Keten, S.; Gilman, J. W. Simultaneously Tailoring Surface Energies and Thermal Stabilities of Cellulose Nanocrystals Using Ion Exchange: Effects on Polymer Composite Properties for Transportation, Infrastructure, and Renewable Energy Applications. *ACS Appl. Mater. Interfaces* **2016**, *8*, 27270−27281.
(18) Beck, S.; Bouchard, J.; Chauve, G.; Berry, R. Controlled Production of Patterns in Iridescent Solid Films of Cellulose Nanocrystals. *Cellulose* **2013**, *20*, 1401−1411.
(19) Dumanli, A. G.; Kamita, G.; Landman, J.; van der Kooij, H.; Glover, B. J.; Baumberg, J. J.; Steiner, U.; Vignolini, S. Controlled, Bio-Inspired Self-Assembly of Cellulose-Based Chiral Reflectors. *Adv. Opt. Mater.* **2014**, *2*, 646−650.
(20) Ureña-Benavides, E. E.; Ao, G.; Davis, V. A.; Kitchens, C. L. Rheology and Phase Behavior of Lyotropic Cellulose Nanocrystal Suspensions. *Macromolecules* **2011**, *44*, 8990−8998.
(21) Schütz, C.; Agthe, M.; Fall, A. B.; Gordeyeva, K.; Guccini, V.; Salajková, M.; Plivelic, T. S.; Lagerwall, J. P. F.; Salazar-Alvarez, G.; Bergström, L. Rod Packing in Chiral Nematic Cellulose Nanocrystal Dispersions Studied by Small-Angle X-Ray Scattering and Laser Diffraction. *Langmuir* **2015**, *31*, 6507−6513.
(22) Mu, X.; Gray, D. G. Droplets of Cellulose Nanocrystal Suspensions on Drying Give Iridescent 3-D "coffee-Stain" Rings. *Cellulose* **2015**, *22*, 1103−1107.
(23) Obrzut, J.; Emiroglu, C.; Kirillov, O.; Yang, Y.; Elmquist, R. E. Surface Conductance of Graphene from Non-Contact Resonant Cavity. *Measurement* **2016**, *87*, 146−151.
(24) Orloff, N. D.; Obrzut, J.; Long, C. J.; Lam, T.; Kabos, P.; Novotny, D. R.; Booth, J. C.; Liddle, J. A. Dielectric Characterization by Microwave Cavity Perturbation Corrected for Nonuniform Fields. *IEEE Trans. Microwave Theory Technol.* **2014**, *62*, 2149−2159.
(25) Waldron, R. A. Perturbation Theory of Resonant Cavities. *Proc. Inst. Electr. Eng., Part C* **1960**, *107*, 272.
(26) Yaghjian, A. D. Augmented Electric- and Magnetic-Field Integral Equations. *Radio Sci.* **1981**, *16*, 987−1001.
(27) Aulin, C.; Ahola, S.; Josefsson, P.; Nishino, T.; Hirose, Y.; Österberg, M.; Wågberg, L. Nanoscale Cellulose Films with Different Crystallinities and Mesostructures—Their Surface Properties and Interaction with Water. *Langmuir* **2009**, *25*, 7675−7685.
(28) Vargas-Lara, F.; Douglas, J. F. Confronting the Complexity of CNT Materials. *Soft Matter* **2015**, *11*, 4888−4898.
(29) Kellogg, O. D. *Foundations of Potential Theory*; Springer: Berlin, 1929.
(30) Sihvola, A. H. *Electromagnetic Mixing Formulas and Applications*; IEE electromagnetic waves series, 1st ed./reprint with new cover; Institution of Engineering and Technology: London, 1999.
(31) Landau, L. D.; Lifšic, E. M.; Pitaevskij, L. P.; Landau, L. D. *Electrodynamics of Continuous Media*; Course of theoretical physics; 2nd ed.; Elsevier: Amsterdam, 2008.
(32) Hasted, J. B. *Aqueous Dielectrics*; Studies in chemical physics; Chapman and Hall: London, 1973.
(33) Artemov, V. G.; Volkov, A. A. Water and Ice Dielectric Spectra Scaling at 0 °C. ArXiv Prepr. ArXiv13081229, 2013.
(34) Majoinen, J.; Kontturi, E.; Ikkala, O.; Gray, D. G. SEM Imaging of Chiral Nematic Films Cast from Cellulose Nanocrystal Suspensions. *Cellulose* **2012**, *19*, 1599−1605.
(35) Roman, M.; Gray, D. G. Parabolic Focal Conics in Self-Assembled Solid Films of Cellulose Nanocrystals. *Langmuir* **2005**, *21*, 5555−5561.
(36) de Gennes, P. G.; Prost, J. *The Physics of Liquid Crystals*; The international series of monographs on physics; 2nd ed.; Clarendon Press: Oxford, 1998.
(37) Owens, D. K.; Wendt, R. C. Estimation of the Surface Free Energy of Polymers. *J. Appl. Polym. Sci.* **1969**, *13*, 1741−1747.

DOI: 10.1021/acsami.7b01674
ACS Appl. Mater. Interfaces XXXX, XXX, XXX−XXX

(38) Uhlig, M.; Fall, A.; Wellert, S.; Lehmann, M.; Prévost, S.; Wågberg, L.; von Klitzing, R.; Nyström, G. Two-Dimensional Aggregation and Semidilute Ordering in Cellulose Nanocrystals. *Langmuir* **2016**, *32*, 442−450.
(39) Wang, P.-X.; Hamad, W. Y.; MacLachlan, M. J. Structure and Transformation of Tactoids in Cellulose Nanocrystal Suspensions. *Nat. Commun.* **2016**, *7*, 11515.
(40) Ličen, M.; Majaron, B.; Noh, J.; Schütz, C.; Bergström, L.; Lagerwall, J.; Drevenšek-Olenik, I. Correlation between Structural Properties and Iridescent Colors of Cellulose Nanocrystalline Films. *Cellulose* **2016**, *23*, 3601−3609.
(41) Araki, J.; Kuga, S. Effect of Trace Electrolyte on Liquid Crystal Type of Cellulose Microcrystals. *Langmuir* **2001**, *17*, 4493−4496.

DOI: 10.1021/acsami.7b01674
ACS Appl. Mater. Interfaces XXXX, XXX, XXX−XXX